Regular Article

Structure-regulated Ru particles decorated P-vacancy-rich CoP as a highly active and durable catalyst for $NaBH_4$ hydrolysis

Shuqing Zhou [a,1], Yuting Yang [a,1], Wanyu Zhang [a], Xianfa Rao [b], Puxuan Yan [a], Tayirjan Taylor Isimjan [c], Xiulin Yang [a,*]

[a] Guangxi Key Laboratory of Low Carbon Energy Materials, School of Chemistry and Pharmaceutical Sciences, Guangxi Normal University, Guilin 541004, China
[b] School of Resources and Environmental Engineering, Jiangxi University of Science and Technology, Ganzhou 341000, China
[c] Saudi Arabia Basic Industries Corporation (SABIC) at King Abdullah University of Science and Technology (KAUST), Thuwal 23955-6900, Saudi Arabia

HIGHLIGHTS

- Ru-cluster decorated P-vacancy-rich CoP is fabricated by a controllable method.
- The $Ru_{9.8}$/*r*-CoP catalyst exhibits high activity and reusability for $NaBH_4$ hydrolysis.
- Abundant P vacancies contribute to the formation of more uniform and smaller Ru clusters.
- The superior performance attributed to the synergy of Ru clusters and CoP support.

GRAPHICAL ABSTRACT

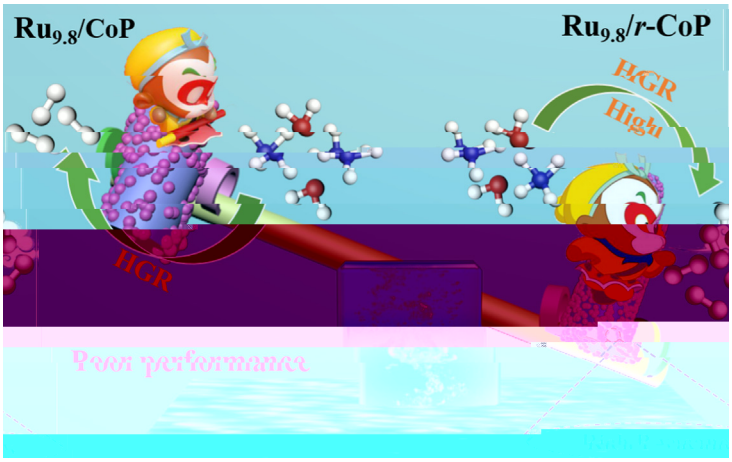

ARTICLE INFO

Article history:
Received 28 November 2020
Revised 23 January 2021
Accepted 2 February 2021
Available online 8 February 2021

Keywords:
Cobalt phosphide
Phosphorus vacancies
$NaBH_4$ hydrolysis
Hydrogen generation

ABSTRACT

$NaBH_4$ is considered the best hydrogen storage material due to its high hydrogen content of 10.6 wt% and good stability. However, $NaBH_4$ hydrolysis requires an efficient catalyst because of the sluggish reaction kinetics. In this work, we have demonstrated a process of preparing a cobalt phosphide-supported Ru particulate nanocatalyst with abundant phosphorus vacancies for the first time. Electron paramagnetic resonance and transmission electron microscopy revealed that the synthesized $Ru_{9.8}$/*r*-CoP catalyst has ample phosphorus vacancies, and Ru species are small particles (~2.5 nm) with uniform dispersion, respectively. More importantly, the optimized $Ru_{9.8}$/*r*-CoP catalyst has the lowest activation energy (45.3 kJ mol^{-1}) and exhibits excellent catalytic performance for $NaBH_4$ hydrolysis with a high hydrogen generation rate 9783.3 $mL H_2$ min^{-1} g_{cat}^{-1} at 25 °C, which is higher than most of the cobalt-based catalysts. Moreover, the $Ru_{9.8}$/*r*-CoP catalyst also shows good reusability. For example, the catalytic performance only declined by *ca.* 14% after

1. Introduction

The overconsumption of fossil energy and the increasing attention to environmental issues have prompted researchers to actively seek renewable energy to replace traditional fossil fuels

technique is used to measured the generated H_2, and the drainage system is connected to a computer to record instantaneous water volume changes. During the reusability study, the catalyst was collected by centrifugation and dried. The collected catalyst from the previous experiment was added to the fresh $NaBH_4$ solution in the next experiment. The catalyst's activation energy was tested in the temperature range from 298 to 318 K, and then calculated by the Arrhenius equation. All tests are repeated three times to ensure reliable results.

The hydrogen generation rate (HGR) and turnover frequency (TOF) values are calculated according to the following equations [34,35],

$$HGR = \frac{V_{H_2O}(mL)}{t(min) \times m(g)} \quad (5)$$

$$TOF = \frac{n_{H_2}(mol)}{t(min) \times n_{Ru}(mol)} \quad (6)$$

where V_{H2O} is the volume of drained water, m is the total mass of the catalyst, n_{H2} is the moles of generated H_2, n_{Ru} is the moles of Ru in the catalyst, and t is the total reaction time in minutes.

$$\ln j = \ln A - E_a/RT \quad (7)$$

Equation (7) is the Arrhenius equation, where j (L min^{-1} g^{-1}) is the hydrogen evolution slope, A (L min^{-1} g^{-1}) is a constant, E_a (kJ mol^{-1}) is the activation energy, R (J mol^{-1} K^{-1}) is the gas constant, and T (K) is the temperature of the during the test.

3. Results and discussion

The synthetic processes of the Ru/r-CoP are illustrated in (Fig. 1a). The CoOOH nanorods were first synthesized by low-temperature hydrothermal methods using cobalt acetate and sodium acetate as precursors combined with PVP as a soft template. The CoOOH precursor template was then placed in a quartz boat and phosphorized in a nitrogen atmosphere at a relatively low temperature of 350 °C. The P vacancies were generated by dispersing the as prepared CoP nanorods into $NaBH_4$ solution (1.5 M). The highly reductive condition generates r-CoP with a large number of phosphorus vacancies. The r-CoP was redispersed in $RuCl_3$ solution, and then the $NaBH_4$ solution (0.08 M) was added dropwise to reduce the Ru^{3+} to form Ru/r-CoP.

As shown in (Fig. 1b), the nanorod-shaped CoOOH was synthesized by low-temperature hydrothermal method (the inset is the SEM with different magnifications). After phosphorized, the morphology of CoP still maintained the original rod-like characteristics (Fig. 1c). However, the surface of r-CoP became rough and porous (Fig. 1d) after treatment with $NaBH_4$ solution. As shown in Fig. 1e and f, the Ru/r-CoP and r-CoP show similar morphology and the Ru particles are uniformly dispersed on the surface of r-CoP (the red circle indicates the position of the Ru particles). The statistical results of about 200 Ru particles concluded that the average particle size is approximately 2.52 nm (Fig. S1 and inset Fig. 1f). In contrast, the Ru particles show an apparent agglomeration on $Ru_{9.8}$/CoP (Fig. 1g). The result indicates that higher surface area and porosity help to disperse the Ru ions thereby prevent the agglomeration during reduction. The high-resolution TEM (HRTEM) image (Fig. 1h) further confirmed the crystal structure of the $Ru_{9.8}$/r-CoP whereas the CoP nanorods show two clear lattice spacing of 0.20 and 0.37 nm, corresponding to the crystal planes of (210) and (101) [36]. Besides, the other two lattice fringes at 0.22 and 0.19 nm are attributed to the (210) and (101) crystal planes of the chemically deposited RuO_2 species, respectively [37] indicating the Ru particles were oxidized upon exposure to the air. The high-angle annular dark-field (HAADF) TEM mapping shows that Ru, Co, P, and O elements are evenly distributed throughout the $Ru_{9.8}$/r-CoP (Fig. 1i).

X-ray diffraction (XRD) pattern is used to explore the crystal structure of different composite materials. As shown in Fig. S2, the crystal structure of the Co-species prepared by the hydrothermal method is consistent with the standard CoOOH diffraction peak [38]. After phosphorization (Fig. 2a), the XRD patterns of the prepared sample are well-matched with the typical CoP diffraction peaks (JCPDS: 29-0497) [39]. Meanwhile, the r-CoP diffraction peaks are consistent with CoP and indicate that a $NaBH_4$ reduction does not affect the crystal structure of the material. Notably, the XRD peak intensity of $Ru_{9.8}$/r-CoP becomes weaker after the reduction and Ru loading. Fig. 2b shows five-strong Raman scattering peaks at 190, 467, 510, 601, and 668 cm^{-1} of all the samples, corresponding to the distinct regions of cobalt oxide, which may be caused by the oxidation of CoP in the air [40].

Furthermore, it is reported that P vacancies generated by $NaBH_4$ treatment [30,31] accelerate the electron transport during the reaction, thereby accelerating the hydrogen evolution process of $NaBH_4$ [41]. We first studied the effect of different concentrations of $NaBH_4$ on the generation of P vacancies. EPR spectrum found that the most substantial unpaired electron peak was produced when $NaBH_4$ concentration was 1.5 M, suggesting that the largest proportion of P vacancies can be generated at g = ~2.08 (Fig. S3). After the Ru-species were modified (Fig. 2c), the EPR intensity was somewhat weakened, which may be due to the Ru-species occupying some of the P defect sites.

The BET specific surface area of $Ru_{9.8}$/r-CoP, r-CoP, and CoP are calculated to be 71.1, 39.6, and 6.6 m^2 g^{-1} (Fig. 2d), along with the adsorption average pore diameters are about 3.48, 3.51, and 2.24 nm, respectively [42]. Compared with CoP, the r-CoP has a larger BET surface area and porosity, which can disperse Ru particles more uniformly. The $Ru_{9.8}$/r-CoP catalyst exhibits the largest BET surface area resulting in smaller Ru particles and more uniform dispersion, consequently providing more active sites and accelerating the transport of solutes and gas emissions compared to other catalysts, thereby improving catalytic performance [43,44].

To understand the catalyst's electronic state changes, we performed XPS characterization (Fig. 3). The XPS full spectra of the catalysts in Fig. S4 indicate the presence of C, O, P, Co, and/or Ru elements, which are consistent with theoretical values. The high-resolution XPS spectra of C 1 s + Ru 3d regions (Fig. 3a) are convoluted into C–C (284.8 eV) and C–O (286.0 eV) used as calibration standards [45,46], and the Ru 3d core levels from $Ru_{9.8}$/r-CoP and $Ru_{9.8}$/CoP are convoluted at the binding energies of 281.1 eV, 282.3 eV (Ru $3d_{5/2}$) and 285.5 eV, 286.7 eV (Ru $3d_{3/2}$) [47,48]. It can be seen that the area ratio of RuO_2 in r-CoP is increased to 73.7% by comparison with CoP (28.2%). The catalyst with a higher RuO_2 content showed a better reaction rate similar to that reported in the recent literature [49,50], revealing that the $NaBH_4$ hydrolysis reaction-rate could be improved significantly through the synergy between the Ru and RuO_2 species in the catalyst. As shown in Fig. 3b, the Co $2p_{3/2}$ regions' peaks at 778.7, 781.6, and 787.1 eV can be ascribed to the Co–P, Co–O, and satellite peak, respectively [51–53]. Notably, except for CoP that has an obvious Co-P peak, all other catalysts' Co-P peaks become so weak that they are not detectable. This result may be because the oxide layer (r-CoP, $Ru_{9.8}$/CoP, and $Ru_{9.8}$/r-CoP) formed on the catalyst's surface that is thicker than the penetration depth of XPS (about 10 nm). It should be emphasized that we can see clear CoP characteristic peaks in the XRD diffraction spectrum (Fig. 2a), which further proves that only the sample surface is oxidized. The existence of such an oxide layer may be one of the reasons for the formation of more homogeneously dispersed RuO_2 species on the surface of r-CoP. The P 2p regions' peaks at 130.29 and 133.79 eV can be

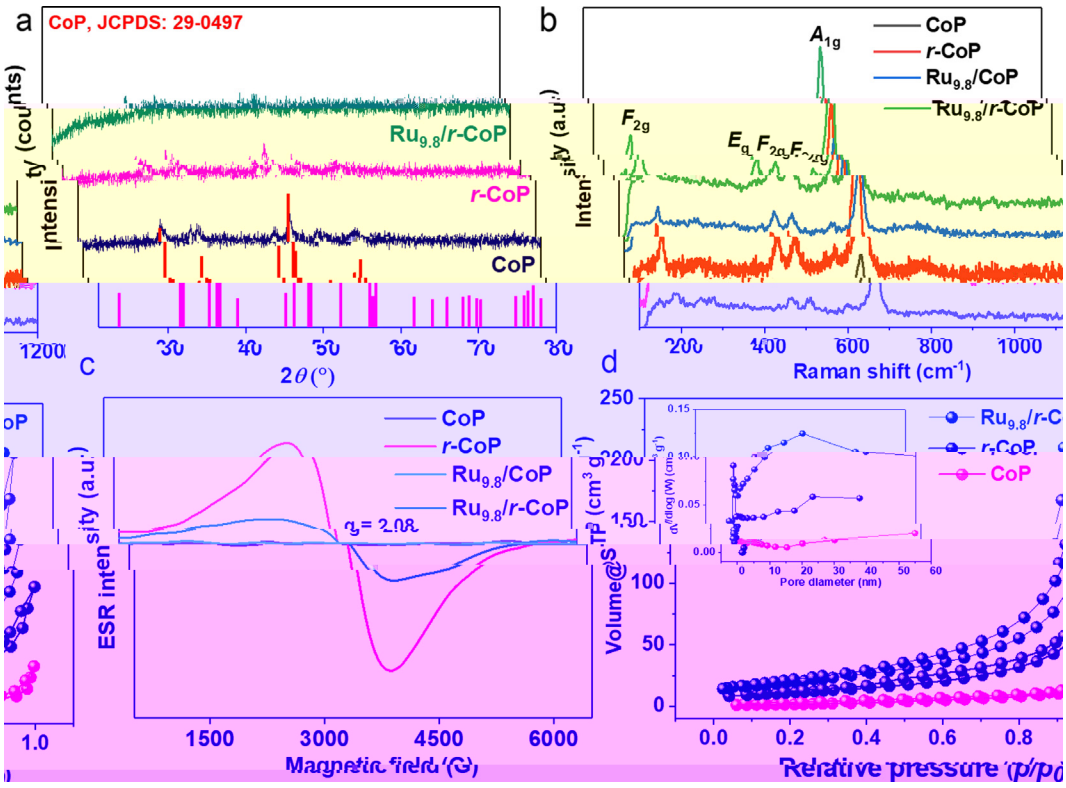

Fig. 2. (a) XRD pattern of CoP, *r*-CoP and $Ru_{9.8}$/*r*-CoP. (b) Raman spectra of CoP, *r*-CoP, $Ru_{9.8}$/CoP and $Ru_{9.8}$/*r*-CoP. (c) EPR spectra of CoP, *r*-CoP, $Ru_{9.8}$/CoP and $Ru_{9.8}$/*r*-CoP. (d) Nitrogen adsorption–desorption isotherms of CoP, *r*-CoP and $Ru_{9.8}$/*r*-CoP.

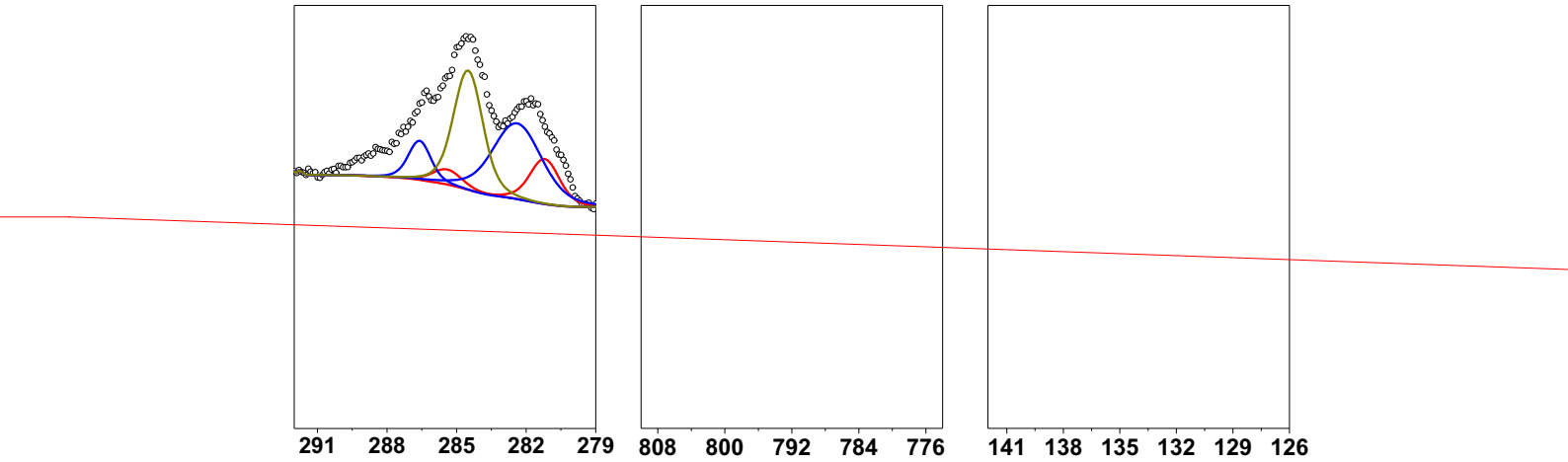

After five cycles, the catalyst remained intact (Fig. S9) and kept the same crystal structure (Fig. S10). However, there is a slight reduction in TOF. However, part of the catalyst deactivation can be attributed to Ru-species exfoliation (Fig. S11) and catalyst poisoning caused by BO_2^- species [59].

The catalytic mechanism diagram of the hydrolysis of $NaBH_4$ solution to hydrogen is proposed in Fig. 6c. The presence of phosphorus vacancies promotes the smaller and more uniformly dispersed Ru particles, consequently increase the grain boundary between the Ru particles and the transition metal phosphide support. Due to the charge transfer from CoP species to Ru resulted from the work function differences (Note: the work functions of Ru is 4.71 eV and CoP is 4.227 eV) [60,61], the Ru becomes electron-rich, thereby selectively binds with B of the BH_4^- ion (Fig. 6c) [62]. Meanwhile, the water is adsorbed by the CoP surface through the P vacancies' binding sites. The adsorbed water molecules can interact with the Ru-BH_4^- at the interface to release one molecule of H_2 and form a BH_3OH intermediate [63,64]. As the reaction proceeds, the rest of the H atoms in the borohydride are replaced by OH^- ions, ultimately dissociating the $B(OH)_4^-$ species [62].

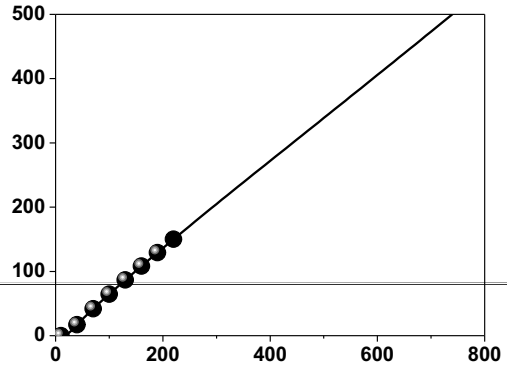
500
400
300
200
100
0
0
200
400
600
800

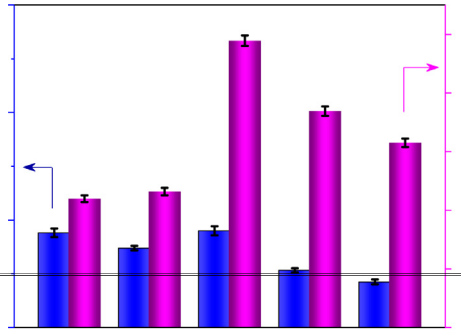

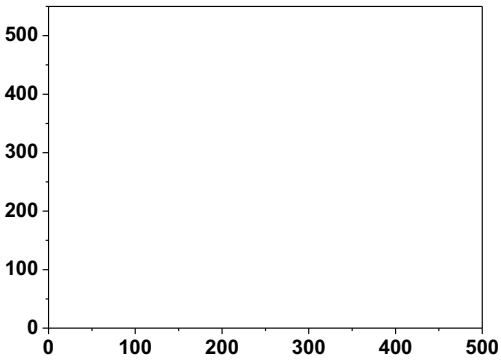
500
400
300
200
100
0
0
100
200
300
400
500

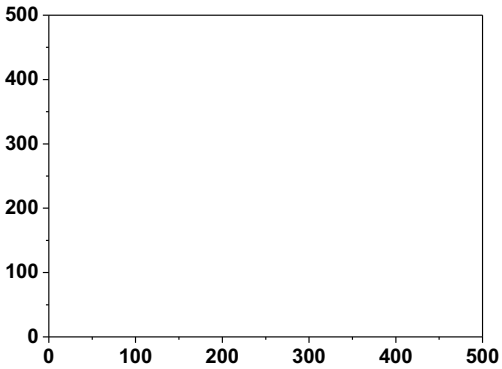
500
400
300
200
100
0
0
100
200
300
400
500

4. Conclusions

In summary, we have successfully developed a facile strategy to prepare Ru particles loaded on r-CoP nanorods that produce H_2 by the hydrolysis of $NaBH_4$ in an alkaline solution. EPR, XPS, and TEM analysis of $Ru_{9.8}$/r-CoP material showed that Ru particles were uniformly dispersed on r-CoP nanorodsÕ surface, thereby creating channels for rapid electron transfer, and full exposure of active sites. The superior performance of $Ru_{9.8}$/r-CoP mainly stems from the following facts. Firstly, the reduced cobalt phosphide has a porous 3D nanorod structure, enhanced BET surface area, and speciÞc pore structure, which provides a good platform for the uniform dispersion of Ru particles. Secondly, the in-situ generated Ru particles on the r-CoP surface have a smaller particle size and expose more active sites induced by P vacancies, thereby obtaining higher catalytic activity. This research provides a new way to develop metal phosphide based a high-performance and low-loading noble metal catalyst for $NaBH_4$ hydrolysis.

CRediT authorship contribution statement

Shuqing Zhou: Writing - original draft. Yuting Yang: Investigation. Wanyu Zhang: Data curation. Xianfa Rao: Data curation. Puxuan Yan: Investigation. Tayirjan Taylor Isimjan: Supervision. Xiulin Yang: Supervision, Writing - review & editing.

Declaration of Competing Interest

The authors declare that they have no known competing Þnancial interests or personal relationships that could have appeared to inßuence the work reported in this paper.

Acknowledgements

This work has been supported by the National Natural Science Foundation of China (no. 21965005), Natural Science Foundation of Guangxi Province (2018GXNSFAA294077, 2018GXNSFAA281220), Project of High-Level Talents of Guangxi (F-KA18015, 2018ZD004), and Guangxi Technology Base and Talent Subject (GUIKE AD18126001).

Appendix A. Supplementary material

Supplementary data to this article can be found online at https://doi.org/10.1016/j.jcis.2021.02.009 .

References

[1] S. Demirci, A.K. Sunol, N. Sahiner, Catalytic activity of amine functionalized titanium dioxide nanoparticles in methanolysis of sodium borohydride for hydrogen generation, Appl. Catal. B: Environ. 261 (2020) 118242 .
[2] J. Lai, S. Guo, Design of ultrathin Pt-based multimetallic nanostructures for efÞcient oxygen reduction electrocatalysis, Small 13 (2017) 1702156 .

[12] B.P.G. Guella, A. Miotello, Kinetic features of the platinum catalyzed hydrolysis of sodium borohydride from 11B NMR measurements, J. Phys. Chem. C 111 (2007) 18744–18750.
[13] O. Sahin, D. Kilinc, C. Saka, Hydrogen generation from hydrolysis of sodium borohydride with a novel palladium metal complex catalyst, J. Energy Inst. 89 (2016) 182–189.
[14] Y.V. Larichev, O.V. Netskina, O.V. Komova, V.I. Simagina, Comparative XPS study of Rh/Al_2O_3 and Rh/TiO_2 as catalysts for $NaBH_4$ hydrolysis, Int. J. Hydrog. Energy 35 (2010) 6501–6507.
[15] D.D. Tuan, K.-Y.-A. Lin, Ruthenium supported on ZIF-67 as an enhanced catalyst for hydrogen generation from hydrolysis of sodium borohydride, Chem. Eng. J. 351 (2018) 48–55.
[16] S.A. Al-Thabaiti, Z. Khan, M.A. Malik, Bimetallic Ag-Ni nanoparticles as an effective catalyst for hydrogen generation from hydrolysis of sodium borohydride, Int. J. Hydrogen Energy 44 (2019) 16452–16466.
[17] C. Wu, J. Guo, J. Zhang, Y. Zhao, J. Tian, T.T. Isimjan, X. Yang, Palladium nanoclusters decorated partially decomposed porous ZIF-67 polyhedron with ultrahigh catalytic activity and stability on hydrogen generation, Renew. Energy 136 (2019) 1064–1070.
[18] S. Akbayrak, M. Kaya, M. Volkan, S. Ozkar, Palladium(0) nanoparticles supported on silica-coated cobalt ferrite: A highly active, magnetically isolable and reusable catalyst for hydrolytic dehydrogenation of ammonia borane, Appl. Catal. B: Environ. 147 (2014) 387–393.
[19] S. Akbayrak, M. Kaya, M. Volkan, S. Ozkar, Ruthenium(0) nanoparticles supported on magnetic silica coated cobalt ferrite: Reusable catalyst in hydrogen generation from the hydrolysis of ammonia-borane, J. Mol. Catal. A Chem. 394 (2014) 253–261.
[20] S. Zhang, Y. Ma, L. Suresh, A. Hao, M. Bick, S.C. Tan, J. Chen, Carbon nanotube reinforced strong carbon matrix composites, ACS Nano 14 (2020) 9282–9319.
[21] J. Chen, D.D. Tune, K. Ge, H. Li, B.S. Flavel, Front and back-junction carbon nanotube-silicon solar cells with an industrial architecture, Adv. Funct. Mater. 30 (2020) 2000484.
[22] Y. Hou, Y.L. Liang, P.C. Shi, Y.B. Huang, R. Cao, Atomically dispersed Ni species on N-doped carbon nanotubes for electroreduction of CO_2 with nearly 100% CO selectivity, Appl. Catal. B: Environ. 271 (2020) 118929.
[23] J. Chen, Z.-H. Lu, Y. Wang, X. Chen, L. Zhang, Magnetically recyclable Ag/SiO_2–$CoFe_2O_4$ nanocomposite as a highly active and reusable catalyst for H_2 production, Int. J. Hydrog. Energy 40 (2015) 4777–4785.
[24] A. Han, H. Chen, Z. Sun, J. Xu, P. Du, High catalytic activity for water oxidation based on nanostructured nickel phosphide precursors, Chem. Commun. 51 (2015) 11626–11629.
[25] L.A. Stern, L.G. Feng, F. Song, X.L. Hu, Ni_2P as a Janus catalyst for water splitting: the oxygen evolution activity of Ni_2P nanoparticles, Energy Environ. Sci. 8 (2015) 2347–2351.
[26] J.M. Wang, Z. Liu, Y.W. Zheng, L. Cui, W.R. Yang, J.Q. Liu, Recent advances in cobalt phosphide based materials for energy-related applications, J. Mater. Chem. A 5 (2017) 22913–22932.
[27] C.Z. Yuan, S.L. Zhong, Y.F. Jiang, Z.K. Yang, Z.W. Zhao, S.J. Zhao, N. Jiang, A.W. Xu, Direct growth of cobalt-rich cobalt phosphide catalysts on cobalt foil: an efficient and self-supported bifunctional electrode for overall water splitting in alkaline media, J. Mater. Chem. A 5 (2017) 10561–10566.
[28] X.C. Zhou, H. Gao, Y.F. Wang, Z. Liu, J.Q. Lin, Y. Ding, P vacancies-enriched 3D hierarchical reduced cobalt phosphide as a precursor template for defect engineering for efficient water oxidation, J. Mater. Chem. A 6 (2018) 14939–14948.
[29] Z. Ran, C. Shu, Z. Hou, P. Hei, T. Yang, R. Liang, J. Li, J. Long, Phosphorus vacancies enriched Ni_2P nanosheets as efficient electrocatalyst for high-performance $Li–O_2$ batteries, Electrochim. Acta 337 (2020) 135795.
[30] X.K. Huang, X.P. Xu, X.X. Luan, D.J. Cheng, CoP nanowires coupled with CoMoP nanosheets as a highly efficient cooperative catalyst for hydrogen evolution reaction, Nano Energy 68 (2020) 104332.
[31] J. Guo, B. Wang, D. Yang, Z. Wan, P. Yan, J. Tian, T.T. Isimjan, X. Yang, Rugae-like Ni_2P-CoP nanoarrays as a bi-functional catalyst for hydrogen generation: $NaBH_4$ hydrolysis and water reduction, Appl. Catal. B: Environ. 265 (2020) 118584.
[32] K.-Y. Niu, L. Fang, R. Ye, D. Nordlund, M.M. Doeff, F. Lin, H. Zheng, Tailoring transition-metal hydroxides and oxides by photon-induced reactions, Angew. Chem. Int. Ed. 55 (2016) 14272–14276.
[33] D. Liu, X. Li, L. Wei, T. Zhang, A. Wang, C. Liu, R. Prins, Disproportionation of hypophosphite and phosphite, Dalton Trans. 46 (2017) 6366–6378.
[34] L. Cui, Y. Xu, L. Niu, W. Yang, J. Liu, Monolithically integrated CoP nanowire array: An on/off switch for effective on-demand hydrogen generation via hydrolysis of $NaBH_4$ and NH_3BH_3, Nano Res. 10 (2017) 595–604.
[35] Q. Yao, Z.-H. Lu, Y. Yang, Y. Chen, X. Chen, H.-L. Jiang, Facile synthesis of graphene-supported Ni-CeO_x nanocomposites as highly efficient catalysts for hydrolytic dehydrogenation of ammonia borane, Nano Res. 11 (2018) 4412–4422.
[36] C. Cai, Y. Teng, J.H. Wu, J.Y. Li, H.Y. Chen, J.H. Chen, D.B. Kuang, In situ photosynthesis of an MAPbI(3)/CoP hybrid heterojunction for efficient photocatalytic hydrogen evolution, Adv. Funct. Mater. 30 (2020) 2001478.
[37] M. Kuang, Y. Wang, W. Fang, H. Tan, M. Chen, J. Yao, C. Liu, J. Xu, K. Zhou, Q. Yan, Efficient nitrate synthesis via ambient nitrogen oxidation with Ru-doped TiO_2 /RuO_2 electrocatalysts, Adv. Mater. 32 (2020) e2002189.
[38] X.L. Yang, H.N. Li, A.Y. Lu, S.X. Min, Z. Idriss, M.N. Hedhili, K.W. Huang, H. Idriss, L.J. Li, Highly acid-durable carbon coated Co_3O_4